Large-Area 2D/3D MoS$_2$–MoO$_2$ Heterostructures with Thermally Stable Exciton and Intriguing Electrical Transport Behaviors

Dawei Li, Zhiyong Xiao, Hossein Rabiee Golgir, Lijia Jiang, Vijay Raj Singh, Kamran Keramatnejad, Kevin E. Smith, Xia Hong, Lan Jiang, Jean-Francois Silvain, and Yongfeng Lu*

To date, scale-up fabrication of transition metal dichalcogenide (TMD-) based 2D/2D or 2D/3D heterostructures with specific functionalities is still a great challenge. This study, for the first time, reports on the controllable synthesis of large-area and continuous 2D/3D semiconductor/metal heterostructures consisting of monolayer MoS$_2$ and bulk MoO$_2$ with unique electrical and optical properties via one-step, vapor-transport-assisted rapid thermal processing. The temperature-dependent electrical transport measurements reveal that the 2D/3D MoS$_2$–MoO$_2$ heterostructure grown on SiO$_2$/Si substrates exhibits metallic phase, while this heterostructure becomes a low-resistance semiconductor when it is grown on fused silica, which is attributed to the different degrees of sulfurization on different substrates, as being confirmed by surface potential analyses. Photoluminescence measurements taken on the MoS$_2$–MoO$_2$ heterostructures reveal the simultaneous presence of both negative trions and neutral excitons, while only neutral excitons are observed in the monolayer MoS$_2$. The trion-binding energy is determined to be ≈27 meV, and the trion signal persists up to 330 K, indicating significant stability at room temperature. This work not only provides a new platform for understanding the intriguing physics in TMD-based heterostructures but also enables the design of more complicated devices with potential applications in nanoelectronics and nanophotonics.

To date, 2D semiconducting transition metal dichalcogenides (TMDs) and TMD-based heterostructures have gained increasing attention as an emerging class of new materials due to their unique aspects and new functionalities in optical, electrical, and chemical properties.[1] The design and fabrication of 2D semiconductor heterostructures stand as a major strategy for the development of various kinds of devices that range from electronics,[2] photovoltaics,[3] sensors,[4,5] spintronics,[6,7] and memories[8] with the intriguing possibility of enhanced performance. For example, TMD (MoS$_2$/WS$_2$) heterostructures exhibit ultrafast charge transfer due to the close proximity of the two heterolayers and the collective motion of excitons at the interface, which enables novel 2D devices for optoelectronics and light harvesting.[9] In the TMD/graphene heterostructures, such hybrid systems exhibit obvious rectification and ambipolar properties with a high field-effect on–off ratio of >10^6 due to the strong interlayer coupling and large band offset between two layers, suggesting their great potentials for future novel optoelectronic devices.[10] Additionally, TMD/graphene heterostructures also demonstrate excellent chemical sensing capability and stability, which provide an essential sensing platform for wearable electronics.[5]

Dr. D. W. Li, H. R. Golgir, Dr. L. J. Jiang, K. Keramatnejad, Prof. Y. F. Lu
Department of Electrical and Computer Engineering
University of Nebraska–Lincoln
Lincoln, NE 68588-0511, USA
E-mail: ylu2@unl.edu
Z. Y. Xiao, Prof. X. Hong
Department of Physics and Astronomy
University of Nebraska–Lincoln
Lincoln, NE 68588-0299, USA
Z. Y. Xiao, Prof. X. Hong
Nebraska Center for Materials and Nanoscience
University of Nebraska–Lincoln
Lincoln, NE 68588-0299, USA

Dr. V. R. Singh, Prof. K. E. Smith
Department of Physics
Boston University
Boston, MA 02215, USA
Prof. K. E. Smith
School of Chemical Sciences
University of Auckland
Auckland 1142, New Zealand
Prof. L. Jiang
School of Mechanical Engineering
Beijing Institute of Technology
Beijing 100081, China
Prof. J.-F. Silvain
Institut de Chimie de la Matière Condensée de Bordeaux
Avenue du Docteur Albert Schweitzer, F-33608 Pessac Cedex, France

**ADVANCED
SCIENCE NEWS**
www.advancedsciencenews.com

**ADVANCED
ELECTRONIC
MATERIALS**
www.advelectronicmat.de

Despite the progress made so far, there are still issues remaining for the controlled fabrication of TMD-based heterostructures. Typical TMD-based heterostructures include 2D/2D vertically stacked and laterally overlapped heterostructures.[11] Mechanical exfoliation [or chemical vapor deposition (CVD)] in conjunction with physical transfer is a popular method for obtaining vertical heterostructures, owing to the better quality and performance. However, multistep exfoliation (or CVD growth) and transfer are required; and these processes carry a serious risk of introducing chemical contamination, poor coupling, and poor reproducibility. Although a hot pick-up technique has been recently developed that enables the rapid batch fabrication of van der Waals (vdW) vertical heterostructure stacks with close to a 100% yield,[12] the smaller effective areas of stacked layers make it difficult to fabricate devices and limit real applications of the technique. The direct one-step (or two-step) CVD methods popularly used for growth of 2D/2D lateral heterostructures,[13] although scalable and relatively simple, encounter similar disadvantages as compared to 2D/2D vertical heterostructure fabrication, i.e., smaller domain sizes and complicated processes for device fabrication.

All the above discussions are limited to all-2D heterostructures. Recently, more complex TMD-based 2D/3D semiconductor heterostructures as one kind of mixed-dimensional vdW heterostructures[14] have also been explored for potential use in hybrid 2D/3D novel electronic and optoelectronic devices.[15–17] A recent example is a 2D/3D p–n junction based on 2D bilayer n-MoS$_2$ and 3D p-Ge, which presents a unique opportunity to realize highly doped p–n junction and resonant tunneling devices for logic applications.[18] In addition, 2D/3D MoS$_2$/Si heterostructures have been investigated for device application such as photodetectors and solar cells.[19,20] More recently, 2D/3D heterostructures based on epitaxially grown MoS$_2$ on GaN substrates have been reported, which present a promising platform for the design of energy-efficient, high-speed, high-power vertical devices incorporating 2D-layered materials with 3D semiconductors.[15] However, MoS$_2$ monolayer coverage is low (only 50% with sheet sizes of only ≈1 µm).[15] Thus, developing robust methods for direct (without physical transfer) and large-scale growth of 2D/3D heterostructures with unique optical and electrical features is an immediate prerequisite. To the best of our knowledge, little has been reported on the direct growth of 2D/3D semiconductor/metal heterostructures. In addition, associated structural, electrical, and optical study is expected to offer a comprehensive approach to fundamental research and practical applications of these novel 2D/3D heterostructures.

In this article, for the first time, we report on the controllable synthesis of large-area and continuous 2D/3D semiconductor/metal heterostructures consisting of monolayer MoS$_2$ and bulk MoO$_2$ via one-step, vapor-transport-assisted rapid thermal processing (VTA-RTP). We then systematically studied the thermal evolution of electrical and optical properties of as-synthesized 2D/3D MoS$_2$–MoO$_2$ heterostructures in comparison with those of as-grown monolayer MoS$_2$. The temperature-dependent electrical transport measurements reveal that the 2D/3D MoS$_2$–MoO$_2$ heterostructure grown on SiO$_2$/Si substrates exhibits metallic phase, while this heterostructure becomes a low-resistance semiconductor when it is grown on fused silica, which is attributed to the different degrees of sulfurization on different substrates, as being confirmed by surface potential analyses. Photoluminescence (PL) measurements taken on the MoS$_2$–MoO$_2$ heterostructures reveal the simultaneous presence of both negative trions (A$^-$) and neutral excitons (A^0 and B), while only neutral excitons are observed in the monolayer MoS$_2$. The trion-binding energy is determined to be ≈27 meV; and the trion still exists at high temperature (≈330 K), indicating significant stability at room temperature. The activation energies extracted from the temperature dependence of A^0 exciton intensity are ≈80 meV for monolayer MoS$_2$ and ≈40 meV for the MoS$_2$–MoO$_2$ heterostructure. This result is consistent with the values obtained from the electrical transport measurements. This work not only provides a new platform for understanding the intriguing physics in TMD-based heterostructures but also enables the design of more complicated devices with potential applications in nanoelectronics and nanophotonics.

We developed a new VTA-RTP method for controllable growth of large-area MoS$_2$-based heterostructures (MoS$_2$–MoO$_2$) and MoS$_2$ thin films (from monolayer to a few layer) (**Figure 1**). Different from the conventional CVD methods, VTA-RTP provides two obvious advantages: (1) time savings due to faster heating/cooling rates (150 °C min^{-1}), and (2) the possibility of quick, nonthermal equilibrium reacting between various precursors for the generation of new low-dimensional materials. The details of the processing conditions can be found in the Experimental Section. Here, two kinds of substrates (SiO$_2$/Si and fused silica) placed downstream with four different precursor–substrate distances were used for the controlled material growth (Figure 1a; Figure S1a, Supporting Information) [For convenience of discussion, the as-synthesized products are labeled as (top, from left to right) P1-SiO$_2$/Si, P2-SiO$_2$/Si, P3-SiO$_2$/Si, and P4-SiO$_2$; and (bottom, from left to right) P1-fused silica, P2-fused silica, P3-fused silica, and P4-fused silica (see Figure S1b-i, Supporting Information)]. Figure 1b and backgrounds in Figure S1b-i (Supporting Information) display optical images of the corresponding samples. We can see that all of the as-synthesized films show uniform color contrast, suggesting homogeneous thickness and continuous films on a large scale.

It is interesting to find that by varying the precursor–substrate distances and the substrate types, the layer number and composition can be well controlled from a monolayer (P4-SiO$_2$/Si) to few-layer MoS$_2$ (P2-SiO$_2$/Si and P3-SiO$_2$/Si) and from pure MoS$_2$ to MoS$_2$-based hybrids (P1-SiO$_2$/Si and P1-fused silica), as evidenced by Raman and PL spectra statistically taken in a large area from each sample (**Figure 2**a,b; Figure S1 and Table S1, Supporting Information). We noted that the normalized PL intensities of the MoS$_2$-based hybrids were exceeding 6 and 3.8, respectively, for P1-SiO$_2$/Si (Figure 2a, black line) and P1-fused silica (Figure 2a, red line). The intensity is much stronger than those of few-layer or thin-film MoS$_2$ (Figure 2b, red line) samples, indicating that a direct bandgap MoS$_2$ monolayer exists in the MoS$_2$-based hybrids.[21] We also observed a red shift of PL peak in the P1-fused silica compared with that in the P1-SiO$_2$/Si, which can be attributed to growth substrate-induced variations in the doping level in MoS$_2$.[22] The Raman spectra of MoS$_2$-based hybrids (inset in Figure 2a) showed that the frequency difference between the E$_{2g}^1$ mode and A$_{1g}$
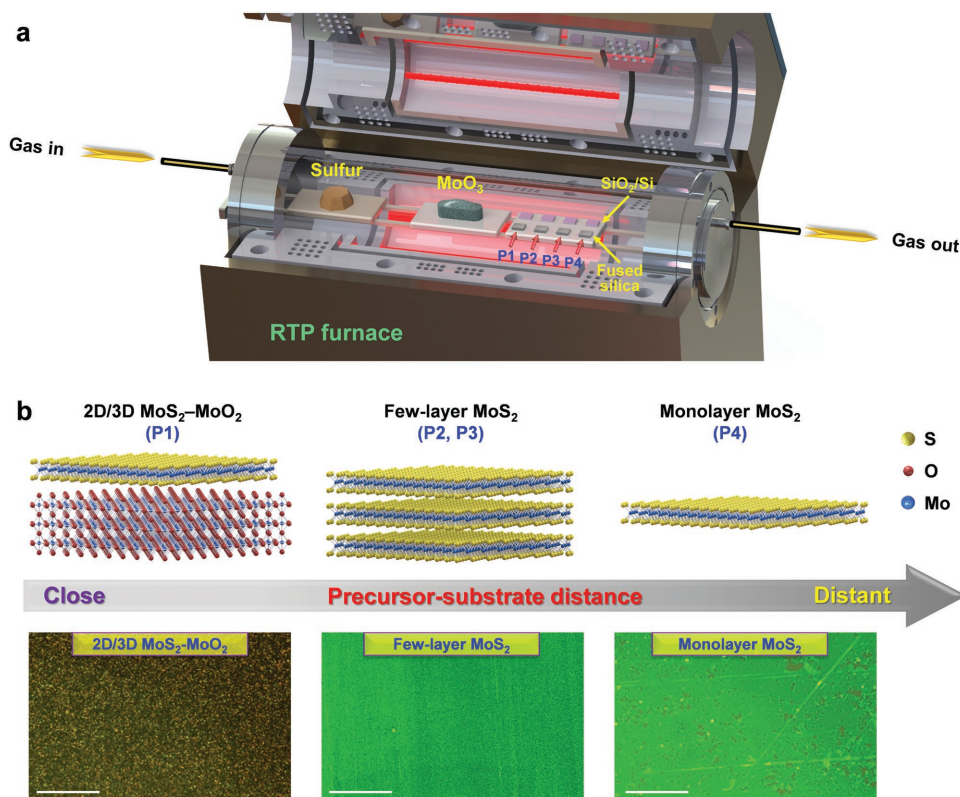
Figure 1. Structure controlled growth of large-area 2D/3D MoS_2–MoO_2 heterostructures and MoS_2 thin films via VTA-RTP. a) Experimental setup of the VTA-RTP system. b) A schematic view (top) and optical micrographs (bottom) showing the structure evolution of growth products, from 2D/3D MoS_2–MoO_2 heterostructure to few-layer and then monolayer MoS_2, by varying the precursor–substrate distance. Scale bars in (b): 40 µm.

mode is ≈20.6 cm^{-1}, further confirming the formation of the monolayer MoS_2 in these two hybrid heterostructures. Comparative Raman analyses in Figure 2c showed that the peak at ≈365 cm^{-1} observed in the inset of Figure 2a, originated from MoO_2, reveals that (1) the MoO_2 is an intermediate product during sulfurization of MoO_3: $S + MoO_3 \rightarrow MoS_2 + MoO_2$, and (2) heterostructures consisting of monolayer MoS_2 and 3D MoO_2 were formed on P1-SiO_2/Si (and P1-fused silica) due to the surface-only sulfurization of MoO_2: $S + MoO_2 \rightarrow MoS_2 + O_2$. This result is similar to the previous report,[23] where MoS_2 atomic layers can be produced by the surface sulfurization of MoO_2 microplates.

X-ray diffraction (XRD) measurements were used to study the phase of the samples (Figure 2d). The XRD peaks for P1-SiO_2/Si (red line) were mainly indexed to monoclinic MoO_2 in space group $P2_1/c$ with the lattice constants of $a = 5.6$ Å, $b = 4.85$ Å, and $c = 5.53$ Å.[24] No peaks of MoO_3 (blue line) or other molybdenum oxides were observed, indicating that MoO_3 was completely reduced into the single-phase MoO_2 in P1-SiO_2/Si, which is consistent with Raman analyses. Unfortunately, no obvious (100) and (110) diffraction peaks for the monolayer MoS_2 could be detected for P1-SiO_2/Si and P4-SiO_2/Si,[25] which could be attributed to their ultrathin layer thicknesses. X-ray photoelectron spectroscopy (XPS) was utilized to further examine the chemical composition and bonding types of the samples (Figure 2e; Figure S2, Supporting Information). Both Mo and S were detected by survey spectra and high-resolution

scans of P1-SiO_2/Si (Figure 2e). From the high-resolution scans of the Mo3d spectrum, we can see three peaks at 225.5, 228.7, and 231.0 eV, corresponding to Mo^{4+}3d, Mo^{4+}3d$_{5/2}$, and Mo^{4+}3d$_{3/2}$; meanwhile the S2p spectrum exhibited only the bonding energies for S^{2-}. These features are the result of MoS_2 and MoO_2 formation in P1-SiO_2/Si, consistent with the XRD and Raman results.

To assess the continuity and uniformity of the as-synthesized films, we performed Raman and PL mappings of two typical samples, monolayer MoS_2 (P4-SiO_2/Si) and MoS_2–MoO_2 heterostructure (P1-SiO_2/Si) (see Figure S3, Supporting Information), demonstrating the excellent uniformity and high crystallinity of MoS_2 and MoS_2–MoO_2 heterostructures grown on a large scale using VTA-RTP. Scanning electron microscopy (SEM) and atomic force microscopy (AFM) were applied to investigate the morphology and structure of the as-synthesized MoS_2–MoO_2 heterostructures and monolayer MoS_2. **Figure 3**a is the SEM image of the MoS_2–MoO_2 heterostructure, which reveals that this film is composed of randomly stacked micro-/nano-polycrystalline (MoO_2) particles [with sharp edges and a lateral size of approximately several hundred nanometers (see Figure S4a, Supporting Information)], forming a continuous 3D structure (Figure 3b). The uniform spatial distributions of Mo, S, and O elements in the MoS_2–MoO_2 heterostructure were identified using SEM/energy-dispersive X-ray spectroscopy (SEM/EDS) (Figure S4, Supporting information), further indicating that the MoS_2
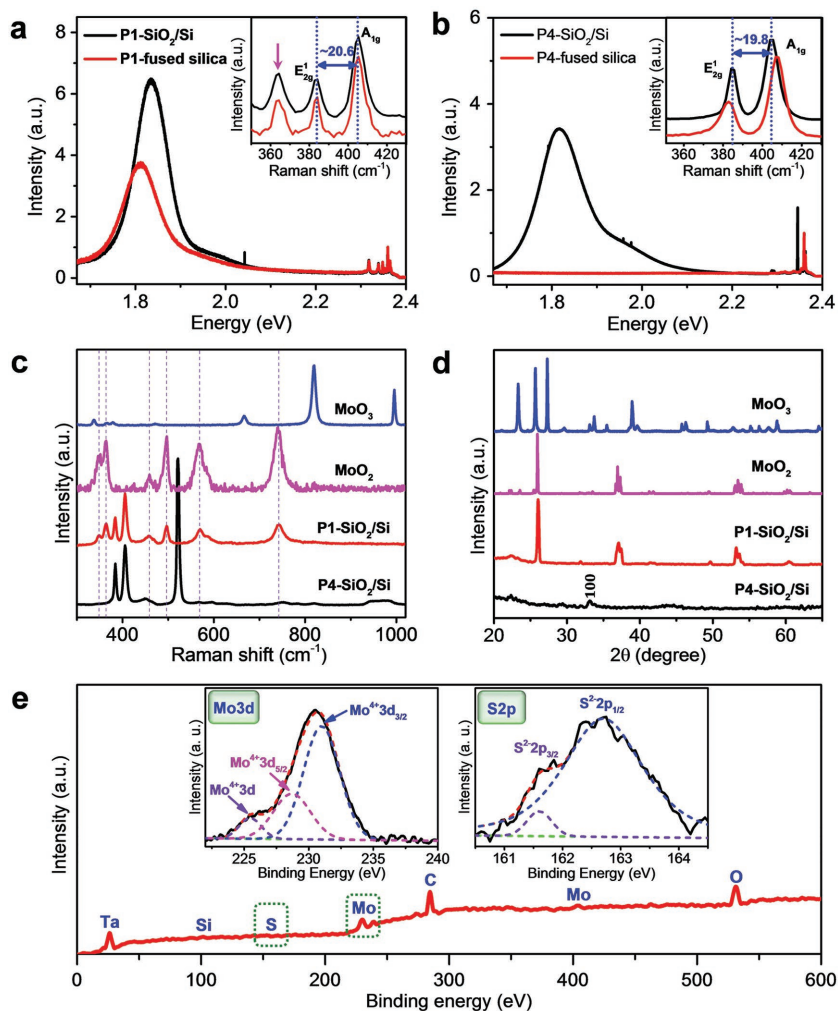
ADVANCED
SCIENCE NEWS
www.advancedsciencenews.com

ADVANCED
ELECTRONIC
MATERIALS
www.advelectronicmat.de

Figure 2. Spectrum characterization. a,b) Representative PL and Raman (inset) spectra measured from samples grown on different substrates with different precursor–substrate distances [(a) P1-SiO$_2$/Si (black line) and P1-fused silica (red line), (b) P4-SiO$_2$/Si (black line) and P4-fused silica (red line)], with PL intensity normalized by Raman A$_{1g}$ peak. c) Raman spectra of the MoS$_2$–MoO$_2$ heterostructure (P1-SiO$_2$/Si) and monolayer MoS$_2$ (P4-SiO$_2$/Si), in comparison with the spectra of pure MoO$_2$ (pink line) and MoO$_3$ (blue line). d) XRD patterns of as-synthesized MoS$_2$–MoO$_2$ heterostructure (red line) and monolayer MoS$_2$ (black line) on SiO$_2$/Si substrates, in comparison with the spectra of pure MoO$_2$ (pink line) and MoO$_3$ (blue line). e) XPS survey spectrum and high-resolution scans (inset) of Mo3d and S2p spectra of MoS$_2$–MoO$_2$ heterostructure.

film was formed and continuously distributed on the surfaces of 3D MoO$_2$, forming the 2D/3D MoS$_2$–MoO$_2$ heterostructures. However, the exact one-step growth mechanism of such novel 2D/3D heterostructures requires further study. The AFM images in both Figure 3d and Figure S5b (Supporting Information) show that the thickness of the MoS$_2$ film (P1-SiO$_2$/Si) is ≈1 nm, further confirming its monolayer characteristics.[26] It is also worth noting that the grain boundaries were observed in as-synthesized monolayer MoS$_2$, indicating that it is a polycrystalline film formed by grain–grain coalescence with a random distribution of lattice orientations. Additionally, the typical grain size in the polycrystalline monolayer MoS$_2$ film is confirmed to be ≈400 nm (see Figure S5b, Supporting Information).

2D/3D semiconductor heterostructures (such as MoS$_2$/Si[17] and MoS$_2$/GaN[15]) have been recently explored, presenting an area of opportunity to extend the functionality of 3D semiconductors. Here, the integration of 2D layered MoS$_2$ with 3D MoO$_2$, forming a new 2D/3D semiconductor/metal heterostructure, is expected to offer more interesting physical properties for designing novel 2D/3D heterostructure-based devices. To demonstrate the potential, we systematically investigated the electrical and optical properties of the as-synthesized 2D/3D MoS$_2$–MoO$_2$ heterostructures in comparison with those of as-grown monolayer MoS$_2$.

Figure S6 (Supporting Information) presented I_{DS}–V_{DS} characterization for (a) monolayer MoS$_2$ and MoS$_2$–MoO$_2$ heterostructures grown on (b) SiO$_2$/Si and (c) fused silica substrates, respectively. The curves of all samples are linear at room temperature and remain linear to low temperatures, indicating an Ohmic contact. We also noted that the source drain current I_{DS} increases as the temperature increases for the monolayer MoS$_2$ and MoS$_2$–MoO$_2$ heterostructures grown on fused silica, while for MoS$_2$–MoO$_2$ heterostructures grown on SiO$_2$/Si, I_{DS} deceases as the temperature increases, reflecting the different phases of MoS$_2$–MoO$_2$ heterostructures grown on different substrates, as will be discussed later in the text.

The electrical properties of monolayer TMD and TMD-based heterostructures are profoundly affected by vacuum/thermal annealing.[19,27] In this work, for monolayer MoS$_2$ (P4-SiO$_2$/Si), after several cycles of vacuum annealing, there was an obvious improvement in sheet resistance from ≈1.35 to ≈0.01 GΩ □$^{-1}$ (see Figure S7, Supporting Information). Therefore, the measurements of the temperature-dependent electrical transport were conducted after several cycles of vacuum annealing since the device has improved and more stable performance with thermal annealing than that without the annealing process (Figure S8, Supporting Information).

Figure 4a shows the temperature dependence of the resistance of a monolayer MoS$_2$. It exhibits a typical semiconducting behavior, with the resistance increasing to a large value as the temperature decreases. Similar behavior was also observed in the thin film MoS$_2$ (see Figure S8b, Supporting Information). For the monolayer MoS$_2$, the conductance, as a function of $1/T$, showed a linear trend at $T > 150$ K (inset in Figure S8a, Supporting Information), suggesting thermally activated conduction. Using the Arrhenius-activation energy model, the conductance can be fitted by

$$G = G_0 \exp[-(E_a/k_B T)] \tag{1}$$

**ADVANCED
SCIENCE NEWS**
www.advancedsciencenews.com

**ADVANCED
ELECTRONIC
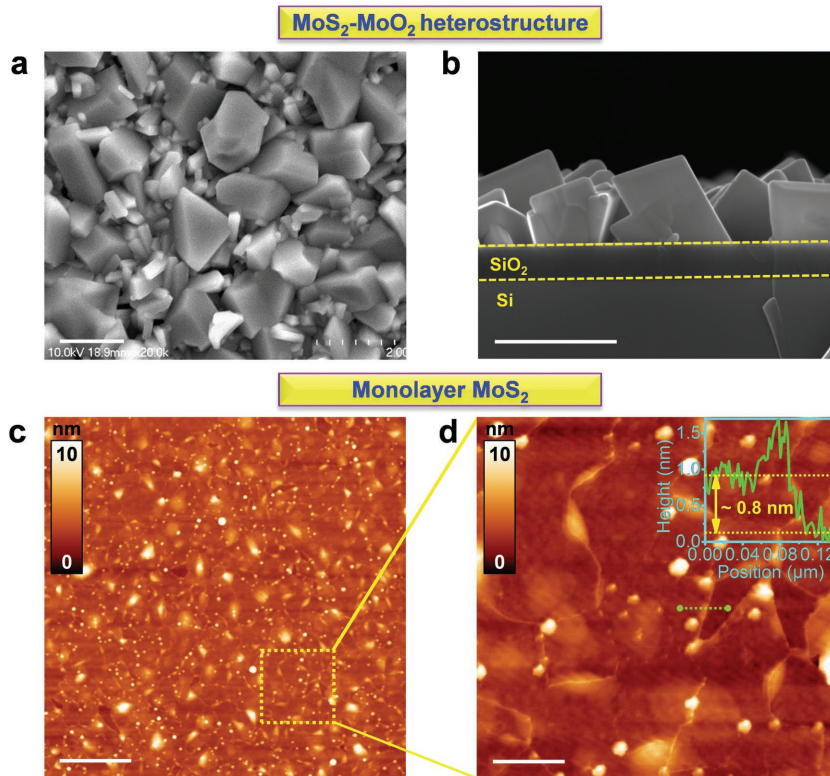MATERIALS**
www.advelectronicmat.de

Figure 3. Structural analyses. a) Top and b) cross-sectional SEM images of MoS₂–MoO₂ heterostructure grown on SiO₂/Si. c) AFM topography and d) magnified view of monolayer MoS₂ grown on SiO₂/Si. The inset in (d) shows the cross-sectional profile along the dashed green line. Scale bars: 1 µm for (a)–(c), 200 nm for (d).

where E_a is the activation energy corresponding to thermal activation of charge carriers at the Fermi energy into the conduction band, k_B is the Boltzmann constant, and G_0 is a fitting parameter, from which we extracted the activation energies E_a of ≈95 and ≈62 meV, respectively, for the monolayer MoS₂ and thin film MoS₂.

We then investigated the MoS₂–MoO₂ heterostructures grown on SiO₂/Si and fused silica substrates, which exhibited significantly different electrical transport properties (Figure 4b,c). For a MoS₂–MoO₂ heterostructure grown on SiO₂/Si, the resistance $R(T)$ showed a metallic behavior, similar to the metallic characteristics of MoO₂ (Figure 4b).[28] The temperature dependence of the resistivity can be well fitted by the Bloch–Grüneisen model which is commonly used in metallic conductor devices

$$R(T) = R(0) + A\left(\frac{T}{\theta_R}\right)^n \int_0^{\frac{\theta_R}{T}} \frac{x^n}{(e^x - 1)(1 - e^{-x})}\,dx \quad (2)$$

where $R(0)$ is the residual resistivity due to defect scattering; A is a constant that depends on the velocity of electrons at the Fermi surface, the Debye radius, and the number density of electrons; θ_R is the Debye temperature; and n is an integer that depends on the nature of the interaction. By fitting the experimental data with the above formula, we obtained a resistivity $R(0)$ of ≈3.69 Ω, constant A of ≈8.94, a Debye temperature θ_R

of ≈709.3 K, and an n of 2, indicating electron–electron interaction in the metallic phase. The MoS₂–MoO₂ heterostructures grown on fused silica, on the other hand, show behavior similar to the monolayer MoS₂, exhibiting a low resistivity in the semiconducting phase (Figure 4c). In addition, we found that neither the Arrhenius nor the Mott variable range hopping (VRH) model can individually describe the $R(T)$ over a wide temperature range.[29] An excellent fit to $R(T)$ can be achieved by including both transport mechanisms[30]

$$G = G_{01} \exp[-(E_a/k_B T)] + G_{02} \exp[-(T_0/T)^{1/2}] \quad (3)$$

where E_a and T_0 represent the activation energy and the hopping energy, respectively; and G_{01} and G_{02} are the corresponding conductance coefficients, indicating that a dual model transport mechanism must be working here. From the fitting, we extracted the activation energy E_a of ≈32 meV and hopping energy T_0 of ≈86 K. Both terms of Equation (3) are plotted in Figure 4c as pink and blue dashed lines, respectively, to show the contributions of each term at different temperature regimes. It is clear that the VRH model dominates at low temperature, while $R(T)$ starts to deviate from the VRH model at a temperature of ≈60 K, suggesting that the thermal activation transport mechanism becomes progressively important at high temperatures.

As we know, 2D/3D MoS₂–MoO₂ heterostructures grown on SiO₂/Si and fused silica substrates have the same components and similar morphologies. The electrical behaviors of two MoS₂–MoO₂ heterostructures should be similar and dominated by the top layer MoS₂, which was contrary to the actual measurement. We conjectured that the different transport characteristics observed in two MoS₂–MoO₂ heterostructures were probably due to the different degrees of sulfurization on different substrates, corresponding to different work functions. To verify our assumption, we performed Kelvin probe force microscope (KPFM), from which the work functions of MoS₂ and MoO₂–MoO₂ heterostructures could be estimated by surface potential measurements. The work functions can be calculated using the following equation

$$\phi_{sample} = \phi_{tip} - eV_{CPD} \quad (4)$$

where ϕ_{sample}, ϕ_{tip}, and V_{CPD} represent the work-functions of the sample, Pt-Ir tip, and the surface potential, respectively. In the insets of Figure 4a–c, we show the KPFM images of (a) monolayer MoS₂ and MoS₂–MoO₂ heterostructures grown on (b) SiO₂/Si and (c) fused silica substrates, from which we obtained the average surface potentials V_{CPD} for each film: 140, −286, and −231 mV, respectively. In this research, the work-function of the Pt-Ir tip was ≈5.4 eV. From the equation above, the work-functions were estimated to be ≈5.3, 5.7, and 5.6 eV,
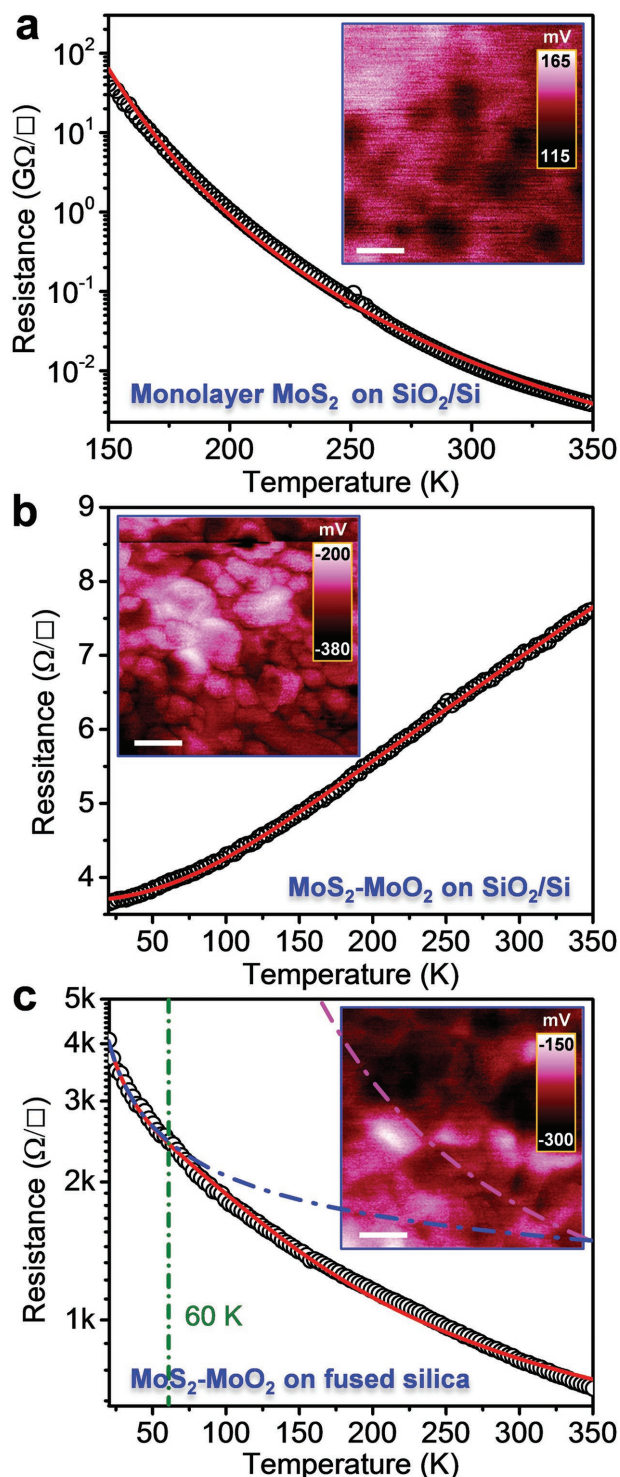
**ADVANCED
SCIENCE NEWS**

www.advancedsciencenews.com

**ADVANCED
ELECTRONIC
MATERIALS**

www.advelectronicmat.de

Figure 4. Temperature-dependent conduction characterization in vacuum. Resistance as a function of temperature for a) monolayer MoS_2 with a fit to Equation (1), b) MoS_2–MoO_2 heterostructure on SiO_2/Si with a fit to Equation (2), and c) MoS_2–MoO_2 heterostructure on fused silica with a fit to Equation (3). Insets in (a)–(c) show KPFM surface potential images for (a) monolayer MoS_2, (b) MoS_2–MoO_2 heterostructure on SiO_2/Si, and (c) MoS_2–MoO_2 heterostructure on fused silica. Scale bars: 400 nm for inset (a) and 1 µm for insets (b) and (c).

respectively, for monolayer MoS_2, MoS_2–MoO_2 heterostructure on SiO_2/Si, and MoS_2–MoO_2 heterostructure on fused silica. In addition, the work-function of metallic MoO_2 was known to be ≈6.5 eV,[31] much higher than that of MoS_2.[32] Based on this analysis, we can deduce that for the MoS_2–MoO_2 heterostructure on SiO_2/Si, which has a larger work-function, its metallic behavior is attributed to a lower coverage of MoS_2 (or insufficient sulfurization) on MoO_2, while sufficient sulfurization in the MoS_2–MoO_2 heterostructure on fused silica with a lower work-function enables its semiconducting behavior. Thus, the ability to phase-engineer 2D/3D MoS_2–MoO_2 heterostructure through substrate, ranging from metallic to semiconducting, could lead to unique electronic transport properties, and open up the possibility for novel electronic devices and architectures.

The temperature dependence of the optical transitions in MoS_2–MoO_2 heterostructures has not been explored in detail. However, this information is very essential to explore the potential applications of 2D/3D semiconductor/metal heterostructures in valleytronics and spintronics. Next, we analyze and compare the exciton behaviors of MoS_2–MoO_2 heterostructures and monolayer MoS_2 using temperature-dependent PL spectroscopy.

Figure 5a,b shows the color mappings of the PL spectra of (a) monolayer MoS_2 and (b) MoS_2–MoO_2 heterostructure as a function of temperature. For monolayer MoS_2, we clearly observed a significant increase in the whole PL intensity when cooling from a high temperature (510 K) down to a low temperature (77 K), which is in agreement with the previous reports of monolayers MoS_2 and $MoSe_2$.[33] A similar trend was also observed in the MoS_2–MoO_2 heterostructure (Figure 5b). This trend can be explained using exciton–photon coupling associated with a large fraction of the excitons lying within the radiative cone at reduced temperature.[34]

Figure 5c,d compares the PL spectra for (c) monolayer MoS_2 and (d) MoS_2–MoO_2 heterostructure measured at 77 K, where the PL spectrum for monolayer MoS_2 can be fitted using a Gaussian model with two peaks and the PL spectrum for the MoS_2–MoO_2 heterostructure can be fitted with three peaks, indicating their distinctly different emission features. We observed that the as-synthesized MoS_2–MoO_2 heterostructure exhibited the simultaneous presence of neutral excitons (A^0 and B) and strong negative trions (A^-) ($A^0 + e \rightarrow A^-$) (Figure 5d),[35] although the trion and A^0 exciton features were not fully resolved because of the relatively high temperature (77 K).[36] While only neutral excitons (A^0 and B) were observed in monolayer MoS_2 (Figure 5c). The energy band diagrams of the three exciton transitions are schematically shown in the inset of Figure 5b. The presence of A^0 and B excitons is attributed to spin–orbit-coupling-induced valence band splitting.[37] The trion observed in the MoS_2–MoO_2 heterostructure is considered due to the existence of a large number of electrons provided by MoO_2. Tersoff model suggested that, for semiconductor/metal heterostructures, the metal atoms can introduce gap states (metal-induced gap states) on the semiconductor side, which will affect the optical response of heterostructures. The energy splitting between A^0 (1.854 eV) and B (2.008 eV) is ≈154 meV in monolayer MoS_2. For the MoS_2–MoO_2 heterostructure, the energies of B, A^0, and A^- are 2.050, 1.918, and 1.889 eV, respectively. Therefore, the energy splitting between

**ADVANCED
SCIENCE NEWS**

www.advancedsciencenews.com

**ADVANCED
ELECTRONIC
MATERIALS**

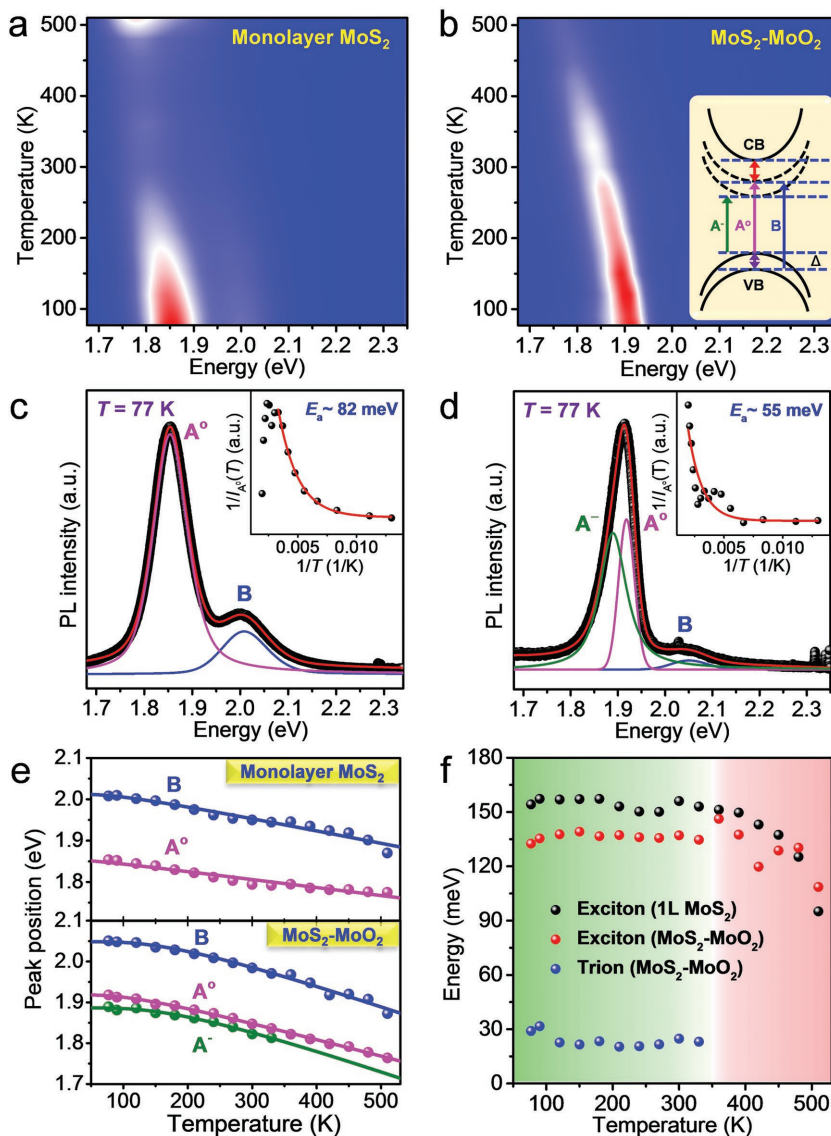www.advelectronicmat.de

Figure 5. Temperature-dependent PL spectra. PL spectra of a) monolayer MoS_2 and b) MoS_2–MoO_2 heterostructure as functions of the temperature. Inset in (b) shows the schematic energy band diagram for atomic MoS_2. Representative PL spectra of c) monolayer MoS_2 and d) MoS_2–MoO_2 heterostructure measured at 77 K, where the black lines are experimental data, pink, blue, and green lines are the fitting curves for the peaks of A^0 excitation, B excitation, and A^- trion, respectively. Insets in (c) and (d) show the corresponding temperature dependence of A^0 exciton PL intensity with a fit to Equation (5). e) Peak position of each exciton (neutral exciton A^0, exciton B, and trion A^-) as a function of temperature for monolayer MoS_2 (top) and MoS_2–MoO_2 heterostructure (bottom) with a fit to Equation (6). f) Temperature dependence of the binding and splitting energy extracted from (e).

A^0 and B is ≈135 meV. The energy difference between trion (A^-) and A^0 is ≈30 meV, very similar to that of monolayer $MoSe_2$ and MoS_2, as previously reported.[37,38]

We then compared the temperature dependence of the extracted A^0 exciton PL intensity for monolayer MoS_2 and the MoS_2–MoO_2 heterostructure, which showed differences (Figure S9 of the Supporting Information and insets in Figure 5c,d). For the MoS_2–MoO_2 heterostructure, the A^0 exciton PL intensity decreased significantly as the temperature increased. For monolayer MoS_2, the A^0 exciton PL intensity first

decreased as the temperature increased (from 77 to 300 K) and then gradually increased as the temperature continued to increase (from 300 to 510 K). Generally, the PL intensity of a semiconductor decreases as the temperature increases due to the thermal activation of nonradiative recombination centers, which model applies well to both samples as the substrate temperature is lower than the room temperature. The fitting functions were plotted using red lines in the insets of Figure 5c,d. The fitting function used is

$$I(T) = \frac{I_0}{1 + A \exp[-(E_a/k_B T)]} \tag{5}$$

where E_a, I_0, and k_B represent the activation energy, A^0 exciton PL intensity at 0 K, and Boltzmann constant, respectively.[39] From the fits, we extracted the activation energies E_a of ≈82 and ≈55 meV for monolayer MoS_2 and MoS_2–MoO_2 heterostructure, respectively. A dramatic decrease in activation energy was observed in the MoS_2–MoO_2 heterostructure, indicating that the excitons in MoS_2–MoO_2 heterostructures have a tendency to dissociate into free carriers as compared to the MoS_2 monolayers.

From the evolution of the extracted trion (A^-) as a function of temperature (see Figure S9d, Supporting Information), we noted that the A^- trion intensity decreased rapidly at ≈200 K, meanwhile the peak width of the A^- trion increased as the temperature increased. Similar to the observed exciton states in $MoSe_2$,[37] the decrease in A^- trion intensity can be attributed to the thermal fluctuations, where the trion is thermally excited to the neutral exciton state ($A^- \rightarrow A^0 + e$). However, it is exciting to note that the trion still exists at a higher temperature (≈330 K) though it becomes relatively weak as compared to A^0 exciton, indicating its significant stability at room temperature. We also found that the $I(A^-)/I(A^0)$ intensity ratio can be effectively controlled, ranging from 2.3 to 0.4, by varying the temperature (Figure S9g, Supporting Information). This is attributed both to the varying thermal fluctuation and the photoionization effect in the MoS_2–MoO_2 heterostructure. Using a standard mass action model, we showed that the temperature dependence of the $I(A^-)/I(A^0)$ intensity ratio can be well fitted, demonstrating a similar but more stable excitonic behavior as compared to that of other 2D semiconductors (such as $MoSe_2$).[37] This effect paves the way to potentially realizing well-controlled excitonic interconnects and high-efficiency valleytronics.[6,38,40]

The effect of temperature on the exciton transition energy (or peak position) was also investigated. As shown in Figure 5e,

ADVANCED
SCIENCE NEWS
www.advancedsciencenews.com

ADVANCED
ELECTRONIC
MATERIALS
www.advelectronicmat.de

the energy positions of all exciton states red-shifted as the temperature increased due to increased electron–phonon interactions as well as slight changes in the bonding length, which was very similar to that observed in the conventional semiconductors.[41] We then used a standard semiconducting bandgap model to quantify the observed behavior. In this model, the exciton energy is

$$E_g(T) = E_g(0) - S\,\hbar\omega\left[\coth\left(\frac{\hbar\omega}{2k_B T}\right) - 1\right] \qquad (6)$$

where $E_g(0)$ is the bandgap value at 0 K, S is a parameter describing the strength of the electron–phonon coupling, and $\hbar\omega$ is the average phonon energy involving in the electron–phonon interaction. We found that this model fits the temperature dependence of neutral excitons and negative trions well. The extracted parameters are summarized in Table S2 of the Supporting Information. Figure 5f displays the temperature dependence of the trion binding energy (estimated from the energy difference between A^0 and A^-) and the excitonic splitting energy between A^0 and B. We can see that the trion binding energy in the MoS_2–MoO_2 heterostructure remains constant, ≈27 meV, over a wide temperature range, indicating a strong Coulomb interaction of the carrier in the semiconductor/metal heterostructures. Similarly, there is no clear temperature dependence of the splitting energy between A^0 and B for both samples when the temperature is lower than 330 K. However, the splitting energy was slightly reduced when the temperature was further increased (from 153 to 95 meV for monolayer MoS_2, and from 135 to 108 meV for the MoS_2–MoO_2 heterostructure), which could be attributed to the screening of the Coulomb interaction at higher temperatures. Overall, the observed large exciton binding energies in MoS_2–MoO_2 would have a significant impact in the next-generation photonics applications based on 2D/3D semiconductor/metal heterostructures.

In summary, we have demonstrated, for the first time, controllable synthesis of 2D/3D semiconductor/metal heterostructures (MoS_2–MoO_2) via a single-step, vapor-transport-assisted rapid thermal processing. As-synthesized 2D/3D heterostructures were composed of semiconducting monolayer MoS_2 and metallic bulk MoO_2 and were continuous in a large scale, as confirmed by a combination of techniques including Raman, PL, XRD, XPS, and SEM. Temperature-dependent electrical transport and PL studies were carried out to explore their unique electrical and optical characteristics. The electrical transport behavior of MoS_2–MoO_2 heterostructures exhibits extreme sensitivity to the degrees of sulfurization. We observed the simultaneous presence of neutral and charged excitons (trions) in the MoS_2–MoO_2 heterostructures via PL spectroscopy, the ratio of which can be effectively controlled by varying the temperature. The trion binding energy is large (≈27 meV) and remains constant over a wide temperature range, indicating a strong Coulomb interaction of carriers in the MoS_2–MoO_2 heterostructures. Our work demonstrated that 2D/3D MoS_2–MoO_2 heterostructures can serve as a promising platform for studying novel physical properties in semiconductor/metal heterostructures

and open up a new avenue for creating 2D TMD-based heterostructures for electronic and optoelectronic devices.

Experimental Section

Controllable Growth of Monolayer MoS₂ and MoS₂–MoO₂ Heterostructures: The VTA-RTP method was developed to realize controllable growth of MoS_2 and MoS_2–MoO_2 heterostructures. The schematic of the VTA-RTP setup is shown in Figure 1a. Sulfur (S) (99.998% trace metals basis, Sigma-Aldrich) and molybdenum oxide (MoO_3) powders (ACS reagent, ≥99.5%, Sigma-Aldrich) were selected as S and Mo precursor sources, respectively. A ceramics (Al_2O_3) boat containing S powder (≈30 mg) was placed in the upstream, and the other Al_2O_3 boat containing MoO_3 powder (≈200 mg) was placed into the center of the RTP tube. Two kinds of substrates (SiO_2/Si and fused silica) placed in downstream with four different precursor–substrate distances (adjacent substrate distance: ≈1 cm) were used for the controllable material growth. The RTP tube was first pumped down and maintained at ≈1.05 Torr. Ar carrier gas with a flow rate of 40 sccm was then introduced to the RTP tube. The temperature of the RTP tube was increased from 20 to 750 °C with a heating rate of 150 °C min⁻¹, kept unchanged at 750 °C for 10 min, and then reduced to room temperature. The samples were taken out for analyses without any further treatments.

Device Fabrication and Temperature-Dependent Electrical Transport Characterization: Devices were fabricated using a standard photolithography and lift-off process. A Ti/Au (5/50 nm) thin film was deposited using e-beam evaporation to form the source and drain electrodes with a channel width of 15 µm. Electrical transport measurements were carried out using the Quantum Design Physical Property Measurement System (PPMS, Quantum Design, Inc., USA) between 20 and 350 K at a vacuum pressure of ≈5 Torr combined with a Keithley 2400 SourceMeter. First, the I_{DS}–V_{DS} curves at different temperatures were measured. The temperature dependence of resistance measurement was then taken at a cooling/heating rate of ≈10 K min⁻¹ in the linear I–V regime, where the resistance value is current-independent.

Raman and PL Measurements: Temperature-dependent Raman and PL spectroscopy was performed in a micro-Raman system (Renishaw InVia plus, Renishaw, Gloucestershire, UK) in combination with a commercial liquid nitrogen heating/cooling chamber (77800 K, THMS600, Linkam Scientific, UK). The excitation source was an Ar⁺ laser with a wavelength of 514.5 nm and a tunable power ranging from ≈3 mW to ≈10 µW. The spot size focused onto the sample was ≈1.5 µm. Raman and PL spectra were collected through a 50× long-focus objective lens with an accumulation time of 10 s.

AFM and KPFM: The AFM and KPFM images were obtained using a Bruker Multimode 8 AFM system. To evaluate and determine the thickness of the samples, an AFM tip (SCANASYST-AIR, Bruker Nano Inc., USA) was applied to probe the topography in the peak-force working mode. The KPFM measurements were performed using a conductive tip (SCM-PIT, Bruker, USA) with a resonant frequency of 75 kHz. During the KPFM measurement, the lift height was 60 nm, and the AC bias was 0.5 V.

SEM and EDS: The surface morphologies and dimensions of as-synthesized samples were studied using a field emission scanning electron microscope (FE-SEM, S4700, Hitachi, Japan). An EDS (Oxford Instruments) mapping was applied to analyze the composition and element distribution in monolayer MoS_2–MoO_2 heterostructures.

XRD: The phase and crystallinity of the samples were examined using a powder X-ray diffractometer (Rigaku D/Max B diffractometer, Co Kα_1 λ = 1.788 Å).

XPS: The chemical composition and bonding types of the samples were studied using a home-built XPS system. The XPS data were collected using a hemispherical analyzer (Scienta Omicron SES-50, VG Scienta, Sweden) with monochromatic X-rays generated by an aluminum $K\alpha$ anode. The base pressure of the vacuum chamber was 5.4×10^{-10}

**ADVANCED
SCIENCE NEWS**

www.advancedsciencenews.com

**ADVANCED
ELECTRONIC
MATERIALS**

www.advelectronicmat.de

Torr during the measurements. The spectra were calibrated against the C 1s signal from adventitious hydrocarbons.

Conflict of Interest

The authors declare no conflict of interest.

Keywords

[1] a) Z. Wenjing, W. Qixing, C. Yu, W. Zhuo, T. S. W. Andrew, *2D Mater.* **2016**, *3*, 022001; b) H. Wang, F. Liu, W. Fu, Z. Fang, W. Zhou, Z. Liu, *Nanoscale* **2014**, *6*, 12250; c) B. V. Lotsch, *Ann. Rev. Mater. Res.* **2015**, *45*, 85.

[2] a) L. Britnell, R. M. Ribeiro, A. Eckmann, R. Jalil, B. D. Belle, A. Mishchenko, Y.-J. Kim, R. V. Gorbachev, T. Georgiou, S. V. Morozov, A. N. Grigorenko, A. K. Geim, K. S. Novoselov, A. H. C. Neto, K. S. Novoselov, *Science* **2013**, *340*, 1311; b) W. J. Yu, Y. Liu, H. Zhou, A. Yin, Z. Li, Y. Huang, X. Duan, *Nat. Nano* **2013**, *8*, 952; c) C.-H. Lee, G.-H. Lee, A. M. van der Zande, W. Chen, Y. Li, M. Han, X. Cui, G. Arefe, C. Nuckolls, T. F. Heinz, J. Guo, J. Hone, P. Kim, *Nat. Nano* **2014**, *9*, 676.

[3] a) N. Flöry, A. Jain, P. Bharadwaj, M. Parzefall, T. Taniguchi, K. Watanabe, L. Novotny, *Appl. Phys. Lett.* **2015**, *107*, 123106; b) Y. Gong, S. Lei, G. Ye, B. Li, Y. He, K. Keyshar, X. Zhang, Q. Wang, J. Lou, Z. Liu, R. Vajtai, W. Zhou, P. M. Ajayan, *Nano Lett.* **2015**, *15*, 6135; c) M. M. Furchi, A. Pospischil, F. Libisch, J. Burgdörfer, T. Mueller, *Nano Lett.* **2014**, *14*, 4785.

[4] P. T. K. Loan, W. Zhang, C.-T. Lin, K.-H. Wei, L.-J. Li, C.-H. Chen, *Adv. Mater.* **2014**, *26*, 4838.

[5] B. Cho, J. Yoon, S. K. Lim, A. R. Kim, D.-H. Kim, S.-G. Park, J.-D. Kwon, Y.-J. Lee, K.-H. Lee, B. H. Lee, H. C. Ko, M. G. Hahm, *ACS Appl. Mater. Interfaces* **2015**, *7*, 16775.

[6] P. Rivera, K. L. Seyler, H. Yu, J. R. Schaibley, J. Yan, D. G. Mandrus, W. Yao, X. Xu, *Science* **2016**, *351*, 688.

[7] M. V. Kamalakar, A. Dankert, J. Bergsten, T. Ive, S. P. Dash, *Appl. Phys. Lett.* **2014**, *105*, 212405.

[8] S. Bertolazzi, D. Krasnozhon, A. Kis, *ACS Nano* **2013**, *7*, 3246.

[9] a) X. Hong, J. Kim, S.-F. Shi, Y. Zhang, C. Jin, Y. Sun, S. Tongay, J. Wu, Y. Zhang, F. Wang, *Nat. Nanotechnol.* **2014**, *9*, 682; b) H. Wang, J. Bang, Y. Sun, L. Liang, D. West, V. Meunier, S. Zhang, *Nat. Commun.* **2016**, *7*, 11504.

[10] a) N. Huo, Z. Wei, X. Meng, J. Kang, F. Wu, S.-S. Li, S.-H. Wei, J. Li, *J. Mater. Chem. C* **2015**, *3*, 5467; b) S. Rathi, I. Lee, D. Lim, J. Wang, Y. Ochiai, N. Aoki, K. Watanabe, T. Taniguchi, G.-H. Lee, Y.-J. Yu, P. Kim, G.-H. Kim, *Nano Lett.* **2015**, *15*, 5017.

[11] a) A. Pant, Z. Mutlu, D. Wickramaratne, H. Cai, R. K. Lake, C. Ozkan, S. Tongay, *Nanoscale* **2016**, *8*, 3870; b) H. Wang, H. Yuan, S. S. Hong, Y. Li, Y. Cui, *Chem. Soc. Rev.* **2015**, *44*, 2664.

[12] F. Pizzocchero, L. Gammelgaard, B. S. Jessen, J. M. Caridad, L. Wang, J. Hone, P. Boggild, T. J. Booth, *Nat. Commun.* **2016**, *7*, 11894.

[13] a) Y. Gong, J. Lin, X. Wang, G. Shi, S. Lei, Z. Lin, X. Zou, G. Ye, R. Vajtai, B. I. Yakobson, H. Terrones, M. Terrones, B. K. Tay, J. Lou, S. T. Pantelides, Z. Liu, W. Zhou, P. M. Ajayan, *Nat. Mater.* **2014**, *13*, 1135; b) C. Huang, S. Wu, A. M. Sanchez, J. J. P. Peters, R. Beanland, J. S. Ross, P. Rivera, W. Yao, D. H. Cobden, X. Xu, *Nat. Mater.* **2014**, *13*, 1096; c) M.-Y. Li, Y. Shi, C.-C. Cheng, L.-S. Lu, Y.-C. Lin, H.-L. Tang, M.-L. Tsai, C.-W. Chu, K.-H. Wei, J.-H. He, W.-H. Chang, K. Suenaga, L.-J. Li, *Science* **2015**, *349*, 524.

[14] D. Jariwala, T. J. Marks, M. C. Hersam, *Nat. Mater.* **2017**, *16*, 170.

[15] D. Ruzmetov, K. Zhang, G. Stan, B. Kalanyan, G. R. Bhimanapati, S. M. Eichfeld, R. A. Burke, P. B. Shah, T. P. O'Regan, F. J. Crowne, A. G. Birdwell, J. A. Robinson, A. V. Davydov, T. G. Ivanov, *ACS Nano* **2016**, *10*, 3580.

[16] E. W. Lee, C. H. Lee, P. K. Paul, L. Ma, W. D. McCulloch, S. Krishnamoorthy, Y. Wu, A. R. Arehart, S. Rajan, *Appl. Phys. Lett.* **2015**, *107*, 103505.

[17] C. Yim, M. O'Brien, N. McEvoy, S. Riazimehr, H. Schäfer-Eberwein, A. Bablich, R. Pawar, G. Iannaccone, C. Downing, G. Fiori, M. C. Lemme, G. S. Duesberg, *Sci. Rep.* **2014**, *4*, 5458.

[18] D. Sarkar, X. Xie, W. Liu, W. Cao, J. Kang, Y. Gong, S. Kraemer, P. M. Ajayan, K. Banerjee, *Nature* **2015**, *526*, 91.

[19] O. Lopez-Sanchez, E. Alarcon Llado, V. Koman, A. Fontcuberta i Morral, A. Radenovic, A. Kis, *ACS Nano* **2014**, *8*, 3042.

[20] B. Li, G. Shi, S. Lei, Y. He, W. Gao, Y. Gong, G. Ye, W. Zhou, K. Keyshar, J. Hao, P. Dong, L. Ge, J. Lou, J. Kono, R. Vajtai, P. M. Ajayan, *Nano Lett.* **2015**, *15*, 5919.

[21] K. F. Mak, C. Lee, J. Hone, J. Shan, T. F. Heinz, *Phys. Rev. Lett.* **2010**, *105*, 136805.

[22] M. Buscema, G. A. Steele, H. S. J. van der Zant, A. Castellanos-Gomez, *Nano Res.* **2014**, *7*, 561.

[23] X. Wang, H. Feng, Y. Wu, L. Jiao, *J. Am. Chem. Soc.* **2013**, *135*, 5304.

[24] B. Hu, L. Mai, W. Chen, F. Yang, *ACS Nano* **2009**, *3*, 478.

[25] a) Y. H. Lee, X. Q. Zhang, W. Zhang, M. T. Chang, C. T. Lin, K. D. Chang, Y. C. Yu, J. T. W. Wang, C. S. Chang, L. J. Li, *Adv. Mater.* **2012**, *24*, 2320; b) P. Joensen, E. D. Crozier, N. Alberding, R. F. Frindt, *J. Phys. C* **1987**, *20*, 4043.

[26] a) B. Radisavljevic, A. Radenovic, J. Brivio, V. Giacometti, A. Kis, *Nat. Nano* **2011**, *6*, 147; b) D. Li, W. Xiong, L. Jiang, Z. Xiao, H. R. Golgir, M. Wang, X. Huang, Y. Zhou, Z. Lin, J. Song, S. Ducharme, L. Jiang, J.-F. Silvain, Y. Lu, *ACS Nano* **2016**, *10*, 3766.

[27] D. Ovchinnikov, A. Allain, Y.-S. Huang, D. Dumcenco, A. Kis, *ACS Nano* **2014**, *8*, 8174.

[28] Y. Shi, B. Guo, S. A. Corr, Q. Shi, Y.-S. Hu, K. R. Heier, L. Chen, R. Seshadri, G. D. Stucky, *Nano Lett.* **2009**, *9*, 4215.

[29] W. Zhu, T. Low, Y.-H. Lee, H. Wang, D. B. Farmer, J. Kong, F. Xia, P. Avouris, *Nat. Commun.* **2014**, *5*, 3087.

[30] K. Zou, J. Zhu, *Phys. Rev. B* **2010**, *82*, 081407.

[31] Y. Liang, C. Tracy, E. Weisbrod, P. Fejes, N. D. Theodore, *Appl. Phys. Lett.* **2006**, *88*, 081901.

[32] S. Choi, Z. Shaolin, W. Yang, *J. Korean Phys. Soc.* **2014**, *64*, 1550.

[33] S. Tongay, J. Zhou, C. Ataca, K. Lo, T. S. Matthews, J. Li, J. C. Grossman, J. Wu, *Nano Lett.* **2012**, *12*, 5576.

[34] L. C. Andreani, F. Tassone, F. Bassani, *Solid State Commun.* **1991**, *77*, 641.

[35] Y. Li, Z. Qi, M. Liu, Y. Wang, X. Cheng, G. Zhang, L. Sheng, *Nanoscale* **2014**, *6*, 15248.

[36] K. F. Mak, K. He, C. Lee, G. H. Lee, J. Hone, T. F. Heinz, J. Shan, *Nat. Mater.* **2013**, *12*, 207.

[37] J. S. Ross, S. Wu, H. Yu, N. J. Ghimire, A. M. Jones, G. Aivazian, J. Yan, D. G. Mandrus, D. Xiao, W. Yao, *Nat. Commun.* **2013**, *4*, 1474.

[38] K. F. Mak, K. He, J. Shan, T. F. Heinz, *Nat. Nanotechnol.* **2012**, *7*, 494.

[39] A. Surrente, A. Mitioglu, K. Galkowski, W. Tabis, D. Maude, P. Plochocka, *Phys. Rev. B* **2016**, *93*, 121405.

[40] M. Baldo, V. Stojanovic, *Nat. Photon.* **2009**, *3*, 558.

[41] K. P. O'Donnell, X. Chen, *Appl. Phys. Lett.* **1991**, *58*, 2924.